



# Multiwavelength Temporal Variability of the Blazar PKS 1510–089

Q. Yuan<sup>1,2</sup>, Pankaj Kushwaha<sup>3,4,15</sup>, Alok C. Gupta<sup>4,5</sup>, Ashutosh Tripathi<sup>6,7</sup>, Paul J. Wiita<sup>8</sup>, M. Zhang<sup>1,9,10</sup>, X. Liu<sup>1,9,10</sup>, Anne Lähteenmäki<sup>11,12</sup>, Merja Tornikoski<sup>11</sup>, Joni Tammi<sup>11</sup>, Venkatesh Ramakrishnan<sup>11,13</sup>, L. Cui<sup>1,9,10</sup>, X. Wang<sup>1,2</sup>, M. F. Gu<sup>5</sup>, Cosimo Bambi<sup>7</sup>, and A. E. Volvach<sup>14</sup>

<sup>1</sup> Xinjiang Astronomical Observatory, Chinese Academy of Sciences, 150 Science 1-Street, Urumqi 830011, People's Republic of China; [yuanqi@xao.ac.cn](mailto:yuanqi@xao.ac.cn)

<sup>2</sup> University of Chinese Academy of Sciences, 19A Yuquan Road, Beijing 100049, People's Republic of China

<sup>3</sup> Department of Physical Sciences, Indian Institute of Science Education and Research Mohali, Knowledge City, Sector 81, SAS Nagar, Punjab 140306, India

<sup>4</sup> Aryabhata Research Institute of Observational Sciences (ARIES), Manora Peak, Nainital 263001, India

<sup>5</sup> Key Laboratory for Research in Galaxies and Cosmology, Shanghai Astronomical Observatory, Chinese Academy of Sciences, 80 Nandan Road, Shanghai 200030, People's Republic of China

<sup>6</sup> Department of Physics, Southern Methodist University, 3215 Daniel Avenue, Dallas, TX 75205, USA

<sup>7</sup> Center for Field Theory and Particle Physics and Department of Physics, Fudan University, 2005 Songhu Road, Shanghai 200438, People's Republic of China

<sup>8</sup> Department of Physics, The College of New Jersey, 2000 Pennington Road, Ewing, NJ 08628-0718, USA

<sup>9</sup> Key Laboratory for Radio Astronomy, Chinese Academy of Sciences, 2 West Beijing Road, Nanjing 210008, People's Republic of China

<sup>10</sup> Xinjiang Key Laboratory of Radio Astrophysics, 150 Science 1-Street, Urumqi 830011, People's Republic of China

<sup>11</sup> Aalto University Metsähovi Radio Observatory, Metsähovintie 114, FI-02540 Kylmäla, Finland

<sup>12</sup> Aalto University Department of Electronics and Nanoengineering, P.O. BOX 15500, FI-00076 Aalto, Finland

<sup>13</sup> Finnish Centre for Astronomy with ESO (FINCA), University of Turku, Vesilinnantie 5, FI-20014 Turku, Finland

<sup>14</sup> Radio Astronomy and Geodynamics Department CrAO, Taras Shevchenko National University of Kyiv, Ukraine

Received 2022 October 9; revised 2023 May 8; accepted 2023 June 9; published 2023 August 1

## Abstract

We perform correlation and periodicity search analyses on long-term multiband light curves of the flat-spectrum radio quasar PKS 1510–089 observed by the space-based Fermi-Large Area Telescope in  $\gamma$ -rays, the SMARTS and Steward Observatory telescopes in optical and near-infrared (NIR), and the 13.7 m radio telescope in Metsähovi Radio Observatory between 2008 and 2018. The  $z$ -transform discrete correlation function method is applied to study the correlation and possible time lags among these multiband light curves. Among all pairs of wavelengths, the  $\gamma$ -ray versus optical/NIR and optical versus NIR correlations show zero time lags; however, both the  $\gamma$ -ray and optical/NIR emissions precede the radio radiation. The generalized Lomb–Scargle periodogram, weighted wavelet  $z$ -transform, and REDFIT techniques are employed to investigate the unresolved core emission-dominated 37 GHz light curve and yield evidence for a quasi period around 1540 days, although given the length of the whole data set it cannot be claimed to be significant. We also investigate the optical/NIR color variability and find that this source shows a simple redder-when-brighter behavior over time, even in the low-flux state.

*Unified Astronomy Thesaurus concepts:* Active galactic nuclei (16); Blazars (164); Flat-spectrum radio quasars (2163); Observational astronomy (1145)

## 1. Introduction

Blazars are radio-loud (RL) active galactic nuclei (AGNs) whose relativistic jets are seen at a small angle to the line of sight (Urry & Padovani 1995). Traditionally, blazars are subclassified as flat-spectrum radio quasars (FSRQs) and BL Lacertae objects (BL Lac objects). There are strong emission lines in the spectra of the former while these lines are weak or absent in the latter. The fluxes from blazars are highly variable in the entire accessible electromagnetic (EM) spectrum, with timescales ranging from minutes to years (e.g., Urry et al. 1993; Petry et al. 2000; Katarzyński et al. 2001; Krawczynski et al. 2001; Aharonian et al. 2002, 2005a, 2005b, 2007, 2009; Błażejowski et al. 2005; Rebillot et al. 2006; Fossati et al. 2008; Horan et al. 2009; Gupta et al. 2017, 2019, 2022; and references therein).

The spectral energy distributions (SEDs) of blazars are characterized by a broad double-peaked structure. The low-

energy hump spans radio to ultraviolet (UV) or X-ray bands with a peak between near-infrared (NIR) and UV/X-ray. This low-energy hump is synchrotron radiation from relativistic nonthermal electrons in the jet. The high-energy hump, on the other hand, extends from X-rays to GeV/TeV  $\gamma$ -rays, peaking between hard X-rays and  $\gamma$ -rays. The origin of the second hump is still unclear; both lepton and hadron based emission scenarios have been proposed (e.g., Böttcher et al. 2013). In leptonic scenarios, the mechanism of the high-energy emission is the inverse Compton (IC) scattering of low-energy seed photons by the same relativistic electrons that produce the synchrotron radiation. Those low-energy seed photons may be the synchrotron photons produced in the jet (synchrotron self-Compton; SSC) or be external photons originating in the local environment (external Compton; EC), including from the accretion disk, the broad-line region (BLR), the dusty torus (DT), or conceivably even the cosmic microwave background (e.g., Tavecchio et al. 2000; Kushwaha et al. 2013; and references therein). In the hadronic scenario, the second hump is due to proton synchrotron radiation or proton-induced particle cascades (e.g., Mannheim & Biermann 1992; Mücke & Protheroe 2001).

Though broadly stochastic in nature, flux variability in the various wave bands differs from source to source. Even for the

<sup>15</sup> DST-INSPIRE Faculty.



same source, there can be significant differences in the correlation of light curves between multiple bands during different observation periods, so studying multiband spectral and temporal variations offers an indirect way to peek into the unresolved processes and spatial scales hidden in compact systems. In general, the emission variability of blazars may be caused by a combination of factors internal to the jet, such as shocks, turbulence, or magnetic reconnection, and external ones, such as changes in the jet direction with respect to the observer (e.g., Böttcher 2019). Blazar variability patterns pose challenges to some existing blazar radiation models and can help discriminate between them.

The location of the  $\gamma$ -ray emission site(s) in blazars has been the subject of substantial debate (e.g., Kushwaha et al. 2013; Hodgson et al. 2017; Arsioli & Chang 2018; Costamante et al. 2018; Acharyya et al. 2021; Kramarenko et al. 2022; and references therein). It is well known that the optical emission of blazars is usually dominated by relativistic jets, but there are exceptions. For example, Fernandes et al. (2020) found that the optical emission in FRSQ 3C 273 was dominated by the accretion disk rather than the jet over the entire time span of their study. A detailed multiwavelength cross-correlation study can analyze the radiation mechanisms in different bands and provide constraints on the location of the  $\gamma$ -ray emitting region(s).

PKS 1510–089 is a bright FSRQ located at redshift  $z = 0.36$  (Thompson et al. 1990; Tanner et al. 1996). It is one of the nine FSRQs detected in the very-high-energy (VHE  $\geq 100$  GeV) range by the Imaging Atmospheric Cherenkov Telescopes (IACTs)<sup>16</sup> and also one of the persistent MeV–GeV emitters (e.g., Kushwaha et al. 2017b). The High Energy Spectroscopic System (H.E.S.S.) collaboration discovered VHE  $\gamma$ -ray emission  $>0.1$  TeV from PKS 1510–089 in 15.8 hr of observation (at  $9.2\sigma$ ; H.E.S.S. Collaboration et al. 2013). The source emitted persistent VHE  $\gamma$ -ray emission in MAGIC observations during its low-flux state for an extended period during 2012–2017 (MAGIC Collaboration et al. 2018). PKS 1510–089 has been subjected to several simultaneous multi-wavelength observing campaigns that obtained flux and spectral variabilities, performed SED modeling, and discussed the diverse emission mechanisms at different epochs of observation (e.g., Kataoka et al. 2008; Abdo et al. 2010; Marscher et al. 2010; Chen et al. 2012; Orienti et al. 2013; Aleksić et al. 2014; Ahnen et al. 2017; and references therein). Recently, transient  $\gamma$ -ray quasiperiodic oscillations (QPOs) with periods of 3.6 and 92 days were reported in Fermi-LAT observations covering  $\sim 12$  yr (Roy et al. 2022b).

PKS 1510–089 has had a substantial amount of well-synchronized sampled data taken in the optical and NIR bands. It is also a target source for numerous blazar radio monitoring programs, such as the Fermi-GST AGN Multi-frequency Monitoring Alliance (F-GAMMA) program (Fuhrmann et al. 2016; Angelakis et al. 2019), the ongoing Owens Valley Radio Observatory (OVRO) 40 m monitoring program (Richards et al. 2011), and the Metsähovi Radio Observatory blazar monitoring program. In addition to these monitoring campaigns, there are quite a few higher-resolution very-long-baseline interferometry (VLBI) observations: the Very Long Baseline Array (VLBA) 2 cm Survey (Kellermann et al. 1998) and its successor Monitoring Of Jets in Active galactic nuclei

with VLBA Experiments (MOJAVE) program (Lister et al. 2018); the VLBA-BU-BLAZAR program and its successor Blazars Entering the Astrophysical Multi-Messenger Era (BEAM-ME) program (Jorstad & Marscher 2016; Jorstad et al. 2017; Weaver et al. 2022). The correlations between different bands have already been studied for PKS 1510–089. Abdo et al. (2010) reported that the  $\gamma$ -ray light curve had a complicated correlation with other wavelengths during the period between 2008 September and 2009 June. They saw no correlation with the X-ray band, a weak correlation with the UV band, and a significant correlation with the optical band, with the  $\gamma$ -ray light curve preceding the optical one by about 13 days. In observations taken during 2009–2013, Beaklini et al. (2017) detected a correlation between the radio and  $\gamma$ -ray flares where the radio flares are delayed by approximately 54 days relative to the  $\gamma$ -ray flares. In another study based on observations taken during 2012 July to 2014 October, the optical and  $\gamma$ -ray bands showed correlations with zero time delay (Ramakrishnan et al. 2016).

Broadband SED studies using multiwavelength data at different source activity states, e.g., 2006 August (Kataoka et al. 2008), 2008 August to 2012 May (Brown 2013), and VHE  $\gamma$ -ray flares in 2009 March (Barnacka et al. 2014) indicate that the radio and optical/NIR emission is synchrotron radiation from the jet, while the high-energy emission (X-ray and  $\gamma$ -ray) arises from the EC scattering of seed photons from the BLR and DT.

This paper focuses on multiband emission connections over lengthy timescales, as we try to understand the blazar radiation mechanisms and jet kinematic behaviors better. Details of the multiband data we include and their reduction procedures for a 10 yr long observation period are provided in Section 2, with a study of spectral variations given in Section 2.5. In Section 3, we present the correlation analysis method and report results among different bands. The subsequent Section 4 deals with the methods used to search for QPOs and the results. We discuss these results in Section 5 and summarize our findings in Section 6.

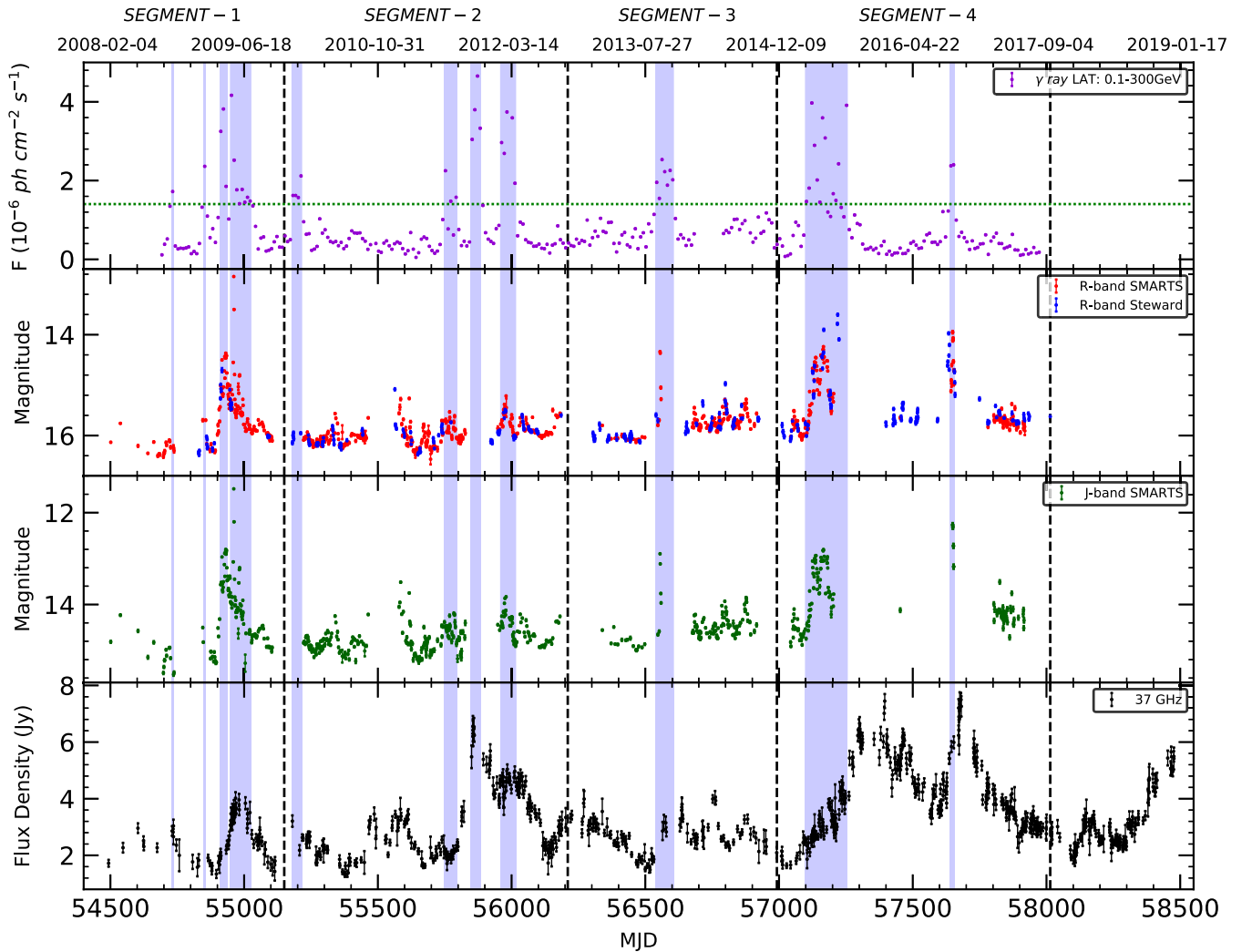
## 2. Multiwavelength Archival Data and Reduction

### 2.1. Fermi $\gamma$ -Ray Data

The Fermi mission is a space-based  $\gamma$ -ray observatory launched in 2008 (Abdo et al. 2010). It is sensitive to  $\gamma$ -ray photons with energies from  $\gtrsim 20$  MeV to  $\sim 1$  TeV. It continuously scans the sky for  $\gamma$ -rays and covers the entire sky region within 90 minutes.

We analyzed the  $\gamma$ -ray data from the Large Area Telescope (LAT) following the standard analysis procedures, employing a “binned likelihood” analysis with the *Fermipy* (v1.0.1) software. We downloaded the PASS8 (P8R3) instrument response function to process data from Fermi-LAT. First, we applied the intended cuts as recommended by selecting only the events marked as “SOURCE” class (evclass = 128 and evtype = 3) with energies above 100 MeV from a region of interest of  $15^\circ$  centered on the source location ( $\alpha_{2000.0} = 15^{\text{h}} 12^{\text{m}} 52^{\text{s}}.2$ ,  $\delta_{2000.0} = -09^\circ 06' 21'' 6$ ). A zenith angle cut of  $90^\circ$  was also applied as recommended by the LAT team. The good time intervals (GTIs) were generated using the standard criteria “(DATA\_QUAL 0)&&(LAT\_CONFIG==1).” For spectral modeling, an XML file with sources from the Fourth LAT Point Source Catalog (4FGL; Abdollahi et al. 2020) was used.

<sup>16</sup> <http://tevcat.uchicago.edu>



**Figure 1.** Multiband light curves of PKS 1510–089 from  $\gamma$ -rays to radio. Vertical lines divide the segments considered for the temporal analysis in our work and the purple-shaded regions represent the  $\gamma$ -ray flaring states. The green horizontal dotted line indicates the constant flux value that divides the high and low  $\gamma$ -ray states.

Apart from the  $\gamma$ -ray emitting point sources, the XML model file also included the galactic and extragalactic isotropic contributions through the template file “lgl\_psc\_v21.fits” and “iso\_P8R3\_SOURCE\_V2\_v1.txt,” provided by the LAT team. The source was modeled with a log-parabola spectrum, as in the catalog. A test statistic (TS) value of  $\geq 9$  was used to select the data for our analysis. The light curve (photon flux versus time) extracted following this procedure is shown in the top panel of Figure 1.

## 2.2. Optical and NIR Data

The optical  $R$ -band data and NIR  $J$ -band data for PKS 1510–089 are taken from the public archives of the Small and Moderate Aperture Research Telescope System (SMARTS)<sup>17</sup> and the Steward Observatory telescopes. SMARTS consists of four meter-class telescopes at the Cerro Tololo Inter-American Observatory (CTIO) in Chile, the 0.9 m, 1.0 m, 1.3 m, and 1.5 m, which observed the Fermi-LAT-monitored blazars at both optical and NIR wavelengths. Details about the SMARTS telescopes, detectors, observations, and data analysis are given in Bonning et al. (2012) and Buxton et al. (2012).

The Steward Observatory of the University of Arizona uses the 2.3 m Bok and 1.54 m Kuiper telescopes to carry out optical photometric and polarimetric observations of a large number of blazars using the spectropolarimeter (SPOL). Details about these telescopes, instruments, observations, and data analysis methods are given in Smith et al. (2009). These  $R$ -band observations are combined with those of SMARTS in the second panel of Figure 1, and the SMARTS  $J$ -band data are in the third panel. Galactic dust reddening and extinction for a line of sight must be considered. The total Galactic visual extinction is estimated and corrected using the extinction map given by Schlegel et al. (1998). Newer estimates of Galactic dust extinction from Schlafly & Finkbeiner (2011) are now provided alongside those of Schlegel et al. (1998). The magnitudes are corrected for galactic extinction using an online tool<sup>18</sup> based on Schlafly & Finkbeiner (2011).

## 2.3. Radio Data

The 37 GHz observations of the blazar PKS 1510–089 were made with the 13.7 m diameter Aalto University Metsähovi radio telescope, which is a radome enclosed Cassegrain type

<sup>17</sup> <http://www.astro.yale.edu/smarts/glast/home.php>

<sup>18</sup> [https://ned.ipac.caltech.edu/extinction\\_calculator](https://ned.ipac.caltech.edu/extinction_calculator)



**Table 1**  
Start and Stop Dates of the Four Individual Segments

SEGMENT	Start Date	Stop Date	Start MJD	Stop MJD
SEGMENT 1	2008 Jan 28	2009 Oct 11	54493	55115
SEGMENT 2	2009 Oct 18	2012 Oct 2	55122	56202
SEGMENT 3	2012 Oct 2	2014 Dec 1	56202	56992
SEGMENT 4	2014 Dec 1	2017 Sep 18	56992	58014

antenna situated in Finland (60° 13′ 04″N, 24° 23′ 35″E). The receivers have high electron mobility pseudomorphic transistor (HEMPT) front ends operating at room temperature. The observations are Dicke switched ON–ON observations, alternating the source and the sky in each feed horn. A typical integration time to obtain one flux density data point is between 1200 and 1800 s. The detection limit of the telescope at 37 GHz is on the order of 0.2 Jy under optimal conditions, but is heavily weather dependent. Data points with a signal-to-noise ratio  $< 4$  are handled as nondetections. The flux density scale is set by observations of the H II region DR 21. Sources NGC 7027, 3C 274, and 3C 84 are used as secondary calibrators. A detailed description of the data reduction and analysis is given in Terasranta et al. (1998). The error estimate of the flux density includes the contribution from the measurement rms and the uncertainty of the absolute calibration. Radio data at 37 GHz are plotted in the bottom panel of Figure 1.

#### 2.4. Multiwavelength Light Curves

Figure 1 shows the multiwavelength light curves of PKS 1510–089 between 2008 and 2018. The aggregated data show frequent changes in the fluxes in different EM bands, with the high (active or flaring) states of the  $\gamma$ -ray fluxes shaded in purple (Figure 1); that shading is extended to the other bands for convenient visualization. To examine the apparent correlations between the variations at different wavelengths in detail, we divide the complete data into four individual segments, denoted by vertical dashed lines, each of which has at least one high  $\gamma$ -ray state and concludes in a gap in the optical/NIR corresponding to the end of an observing season. These segments are chosen to be long enough to allow for the detection of possible changes in correlations between the different bands, as seen in our earlier work (e.g., Gaur et al. 2014; Gupta et al. 2017; Kushwaha et al. 2017a, 2018a, 2018b).

The start and stop dates of the individual segments are given in Table 1. The flaring states’ start and end times within each segment define the subsegments that are listed in Table 2. There are a variety of ways to decide which data points belong to the high and low (quiescent) states (Meyer et al. 2019; Prince et al. 2019; e.g., fractional rms variability, Bayesian blocks, etc.). Here we follow the work of Kushwaha et al. (2016) who showed that the  $\gamma$ -ray flux distribution of PKS 1510–089 showed two distinct log-normal profiles, one for the high-flux level and one for the low one. The intersection of these two log-normal fits, at  $10^{-5.853} = 1.401 \times 10^{-6} \text{ ph cm}^{-2} \text{ s}^{-1}$ , is taken as the separation between flux levels and is shown as a green horizontal dotted line running across panel (a) of Figure 1. A quick look also reveals that the flux changes in different bands are apparently concurrent (except for the radio) and a more careful inspection also shows that the degree of change differs between the EM bands. We must note that data in different EM bands are extracted using different time-bin

durations and thus, are not strictly simultaneous. For example, at  $\gamma$ -ray energies, a 10 day duration is used to ensure sufficient counts for a data point, while such good measurements take just a few minutes for the optical and NIR bands.

##### 2.4.1. Segment 1 (MJD 54493–MJD 55115)

The first segment includes four flaring states. Visual inspection of the multiwavelength light curves shows a close correlation between the  $\gamma$ -ray, optical, NIR, and radio emissions. The optical and NIR bands also brighten during the high activity of the last three  $\gamma$ -ray high states. The observed increase in radio flux seems to start quasi-simultaneously with the third  $\gamma$ -ray high state and reached its peak during the period of the fourth  $\gamma$ -ray high state.

##### 2.4.2. Segment 2 (MJD 55122–MJD 56202)

The source showed intense activity in this period, with four major  $\gamma$ -ray flaring states. The normalized variability amplitudes are not consistent between the bands. In addition, there are seasonal gaps in the optical and NIR light curves during the third of the four  $\gamma$ -ray flaring states due to the target’s proximity to the Sun. Therefore, it is difficult to tell by inspection whether there are any correlations between the different bands.

##### 2.4.3. Segment 3 (MJD 56202–MJD 56992)

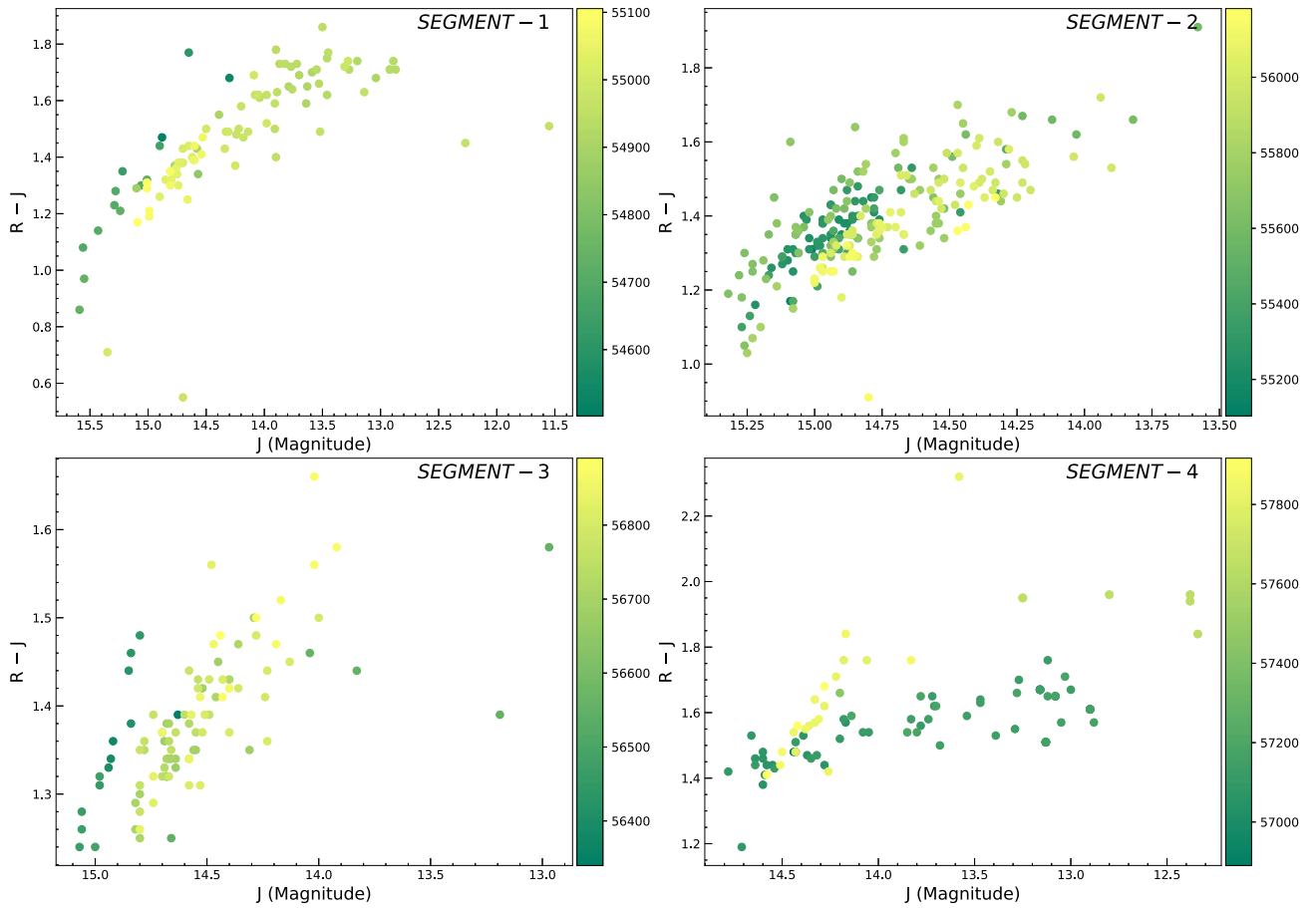
In this segment, the fluctuating trends in the optical and NIR light curves visually coincide with the single  $\gamma$ -ray flaring state but the radio flux density is not as clearly correlated.

##### 2.4.4. Segment 4 (MJD 56992–MJD 58014)

During the first high state of segment 4, four rapid subflares were already identified as A (MJD 57100 to MJD 57150), B (MJD 57150 to MJD 57180), C (MJD 57208 to MJD 57235), and D (MJD 57235 to MJD 57260) in Prince et al. (2019). The four flares described in their paper appear as four peaks in our  $\gamma$ -ray light curve constructed using the 10 day bins. During the high-state period, the optical and NIR emissions also exhibit rapid and complex variations. Visual inspection shows that the first three  $\gamma$ -ray radiation peaks appear almost quasi-simultaneously in the optical band, while the first two peaks also appear almost quasi-simultaneously in the NIR band. Meanwhile, it can be clearly seen that the strong  $\gamma$ -ray emission occurs during the rising phase of the radio outburst. During the second high state of segment 4, there are three near-simultaneous low-frequency counterparts to the  $\gamma$ -ray flaring state. The prominent radio flare shows longer rise and decay timescales than the  $\gamma$ -ray and optical bands.

#### 2.5. Spectral Variations

We calculate the  $(R - J)$  color index of the data sets to examine color variability. Some studies indicate that the observed optical/NIR color changes depending on the current combination of the relativistic jet’s synchrotron emission and the accretion disk’s thermal emission (Isler et al. 2017; Sarkar et al. 2019). Compared to the complex color trends found in studies of some other blazars, PKS 1510–089 shows a simple color behavior. It is clear that the color trends of all segments exhibit a redder-when-brighter (RWB) behavior (Figure 2), i.e., the color index increases with increasing brightness.



**Figure 2.** Color index ( $R - J$ ) vs.  $J$  magnitude in each segment; the color bars indicate the progression of time in MJD.

**Table 2**  
Each Subsegment is Defined as the Start and the End Times of the High State of  $\gamma$ -Ray Emission

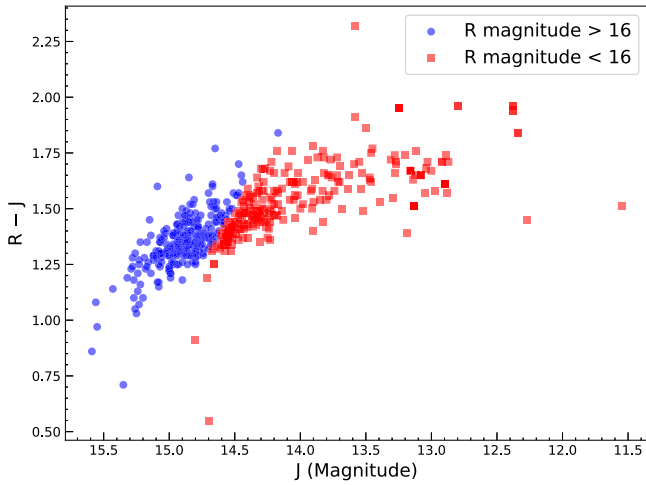
		Start Date	Stop Date	Start MJD	Stop MJD
SEGMENT 1	SEGMENT 1-1	2008 Sep 18	2008 Sep 28	54727	54737
	SEGMENT 1-2	2009 Jan 16	2009 Feb 16	54847	54857
	SEGMENT 1-3	2009 Mar 17	2009 Apr 16	54907	54937
	SEGMENT 1-4	2009 Apr 26	2009 Jul 15	54947	55027
SEGMENT 2	SEGMENT 2-1	2009 Dec 12	2010 Jan 21	55177	55217
	SEGMENT 2-2	2011 Jul 5	2011 Aug 24	55747	55797
	SEGMENT 2-3	2011 Oct 13	2011 Nov 22	55847	55887
	SEGMENT 2-4	2012 Jan 31	2012 Mar 31	55957	56017
SEGMENT 3	SEGMENT 3-1	2013 Sep 2	2013 Nov 11	56537	56607
SEGMENT 4	SEGMENT 4-1	2015 Mar 16	2015 Aug 23	57097	57257
	SEGMENT 4-2	2016 Sep 6	2016 Sep 26	57637	57657

We arbitrarily define the low state as when the  $R$ -band magnitude is greater than 16, and vice versa as the high state. During the optical low-state observation periods, the  $R$ -band and  $J$ -band light curves do not vary rapidly or drastically. When the optical emission is in its low state, the accretion disk emission can dominate and the accretion disk luminosity fluctuates over a wide range of timescales (Lira et al. 2011). Therefore, we investigate the correlation between the  $(R - J)$  color index and the  $J$  magnitude from another perspective using the above state division, which is displayed in Figure 3.

### 3. Variability Analysis and Results

#### 3.1. Method

Traditional timing analysis requires that a time series is sampled evenly in the time domain. In astronomical observations, due to the observation schedule, weather, and technical issues, it is more common that the sampling of the light curve of each campaign is uneven. We apply the  $z$ -transformed discrete correlation function (ZDCF) method (Alexander 1997, 2013) to search for a correlation and time lag between the light curves of each pair of



**Figure 3.** Color index ( $R - J$ ) vs.  $J$  magnitude, grouped by into low-flux states ( $R$  magnitude  $> 16$ , blue circles) and high-flux states ( $R$  magnitude  $< 16$ , red squares).

bands. This method uses equal population binning and Fisher’s  $z$ -transform (Kendall & Stuart 1969, 1973, and references therein) to correct several biases of the discrete correlation function (DCF) method (Edelson & Krolik 1988). This method also ensures that the statistical significance of each bin is high enough by changing the bin width, a form of adaptive binning. The specific binning algorithm we used is described in detail in Kramarenko et al. (2022). After binning, the Pearson’s correlation coefficient ( $r$ ) is calculated and transformed to  $z$ -space:

$$z = \frac{1}{2} \log \left( \frac{1+r}{1-r} \right), \quad \zeta = \frac{1}{2} \log \left( \frac{1+\rho}{1-\rho} \right), \quad r = \tanh z, \quad (1)$$

where  $\rho$  is the unknown population correlation coefficient of the bin. The ZDCF method uses the Ansatz that  $\rho = r$  for the transformation.

The mean of  $z$  ( $\bar{z}$ ) and the variance of  $z$  ( $s_z^2$ ) are estimated by:

$$\bar{z} = \zeta + \frac{\rho}{2(n-1)} \times \left[ 1 + \frac{5 + \rho^2}{4(n-1)} + \frac{11 + 2\rho^2 + 3\rho^4}{8(n-1)^2} + \dots \right], \quad (2)$$

and

$$s_z^2 = \frac{1}{n-1} \left[ 1 + \frac{4 - \rho^2}{2(n-1)} + \frac{22 - 6\rho^2 - 3\rho^4}{6(n-1)^2} + \dots \right]. \quad (3)$$

The error on the ZDCF values is determined from 300 Monte Carlo simulations where light curves are generated by randomly adding an error to each data point according to its observed error, followed by finding their ZDCF estimates. The mean and variance are then estimated in  $z$ -space, which is then transformed back to real space to estimate the error (see Equation (8) of Alexander 2013).

To estimate the significance of the correlation coefficients, we follow the Monte Carlo method described by Max-Moerbeck et al. (2014b) based on the simulated light curves having variability and statistical properties similar to the observed light curve. In this work, we simulated a total of 1000 light curves with the same power spectral density (PSD) and

probability density function (PDF) as the observed light curve in each band using the algorithm presented by Emmanoulopoulos et al. (2013), as realized by the DELightcurveSimulation code (Connolly 2015).<sup>19</sup> We estimate the underlying PSD by fitting a smoothly bending power-law (PL) model plus a constant,  $c$ :

$$\mathcal{P}(f; \gamma, c) = \frac{A f^{-\alpha_{\text{low}}}}{1 + (f/f_{\text{bend}})^{\alpha_{\text{high}} - \alpha_{\text{low}}}} + c, \quad (4)$$

where  $\gamma = (A, f_{\text{bend}}, \alpha_{\text{low}}, \alpha_{\text{high}})$  represents the model parameters, which are the normalization, bend frequency, low-frequency slope, and high-frequency slope, respectively, and  $c$  is an additional Poisson noise constant. The optimal parameters of this PSD model were obtained by maximum likelihood using the Basin-Hopping algorithm and the Nelder-Mead minimization algorithm provided by the Python package SciPy. As for the PDF model, we use a mixed distribution model consisting of a gamma distribution and a log-normal distribution:

$$f_{\text{mix}}(x) = w_{\Gamma} \frac{\theta^{-\kappa} e^{-x/\theta} x^{\kappa-1}}{\Gamma(\kappa)} + w_{\ln \mathcal{N}} \frac{e^{-(\ln x - \mu)^2 / (2\sigma^2)}}{\sqrt{2\pi x \sigma}}, \quad (5)$$

where  $\kappa$  and  $\theta$  are the shape and the scale parameters of the gamma distribution,  $\mu$  and  $\sigma^2$  represent the mean and the variance of the log-normal distribution, and  $w_{\Gamma}$  and  $w_{\ln \mathcal{N}}$  are the weights of the two distributions, respectively, where their sum is 1. The optimal PDF model parameters are obtained through a maximum likelihood analysis using the Broyden-Fletcher-Goldfarb-Shannon minimization algorithm in the Python package SciPy. Table 3 lists the best-fit parameters for both models across all bands.

We calculated the correlation coefficients between the simulated light curves in the exact same way as done for the observed data. After that, the significance levels of the observed data correlation coefficients are derived from the distribution of simulated correlation coefficients for each time lag. It should be noted that significance estimated this way assumes completely random variations in the different bands, which is not true; e.g., the NIR  $J$  and optical  $R$  bands both are dominated by the same synchrotron component. Similarly, the  $\gamma$ -ray fluxes are related to the optical ones if the same particle distribution is responsible for both the synchrotron and IC components. The synchrotron radio emission probably has contributions from a much bigger region and also encodes opacity effects. Thus, the quoted significances are overestimates in general.

### 3.2. Results

The ZDCF results for the entire span of these observations and for the four individual segments are shown in Figures 4 and 5, respectively. The time lags at which the ZDCFs peak are reported in Table 4. Any ZDCF peak within the sampling time resolution is not considered to indicate an actual time lag between the two bands’ emissions. We only consider the highest ZDCF peak closest to 0 lag and discard any peaks near the edges of the temporal span considered (e.g.,  $\pm 300$  days for segment 1).

<sup>19</sup> <https://github.com/samconnolly/DELightcurveSimulation>

**Table 3**  
The Best-fit Parameters for Both Models Across All Bands

Band	PSD					PDF					
	A (Hz <sup>-1</sup> )	f <sub>band</sub> (Hz)	α <sub>low</sub>	α <sub>high</sub>	c (Hz <sup>-1</sup> )	κ	θ	μ	σ	w <sub>Γ</sub>	w <sub>lnN</sub>
γ-rays	22.8056	0.0070	0.1202	1.7735	0.1288	5.9916	6.01437	0.7580	4.5668	0.0994	0.9006
R	0.0814	0.1789	0.8749	5.8442	0.0542	3.8340	0.7921	0.2269	1.3622	0.4850	0.515
J	0.1263	0.1048	0.9620	2.6107	0.0293	3.0122	1.5823	0.2814	2.1324	0.6625	0.3375
37 GHz	3.4348	0.0015	0.3314	1.8827	0.0070	5.3792	0.6663	0.1914	2.741	1.1674	-0.1674

### 3.2.1. Interband Correlations over the Entire Time

We first consider interband correlations over the entire span of these observations. We find correlations close to zero lag with significance larger than  $2\sigma$  between all frequency bands except for  $\gamma$ -rays and 37 GHz, with four of them exceeding  $3\sigma$ :  $\gamma$ -rays and R band,  $\gamma$ -rays and J band, R band and J band, and R band and 37 GHz (Figure 4). The result that these ZDCF peaks near zero lag rarely exceed 0.5 can be understood as the cumulative effect of incorporating the gaps in the R- and J-band data between each segment. We know that even for the same blazar, there can be significant differences in multiband correlations during different observational intervals. Therefore, we study the correlation of light curves between the different bands over the four segments described above, thereby hoping to minimize the impact of missing data on the intrinsic correlations.

### 3.2.2. Interband Correlations for Each Segment

We now consider the results for each segment in examining the correlations between the bands. In most cases, the significance of the highest peak ZDCF peak closest to zero lag is greater than  $2\sigma$  and has a value exceeding 0.6.

*γ-rays versus optical/NIR:* there are significant correlations between the  $\gamma$ -ray photon flux and the optical R-band and NIR J-band flux densities for all segments. Recall that we use a time bin of 10 days to reconstruct the  $\gamma$ -ray light curve. The results given in the first two rows of Figure 5 and Table 4 show that all these ZDCF peaks are within that 10 day interval and hence we measure essentially no time lag between the  $\gamma$ -ray and optical/NIR emissions in every segment.

*γ-rays versus radio:* the  $\gamma$ -ray versus radio ZDCF peaks at nonzero time lags in the first two segments, with the  $\gamma$ -ray emission leading the radio emission by about 50 days in segment 1 and about 40 days in segment 2. In segments 3 and 4, no statistically robust correlations between the  $\gamma$ -ray and 37 GHz bands is seen.

*Optical versus NIR:* for all segments, the optical versus NIR ZDCF peaks have very close to zero time lags, indicating that the R-band and J-band emissions are simultaneous or at least that any delay between these two light curves occurs on a timescale smaller than the cadence of observations.

*Optical/NIR versus radio:* in segment 1 and segment 3, both the optical and NIR versus radio ZDCF peaks correspond to about 40 days, with the optical/NIR emission leading the radio emission. During the MJD 55800–55900 portion of segment 2 the radio emission rises rapidly, and optical and NIR data for this period happen to be missing because of the source’s proximity to the Sun. Therefore it is not surprising that the ZDCF peak for segment 2 shows only a weak correlation

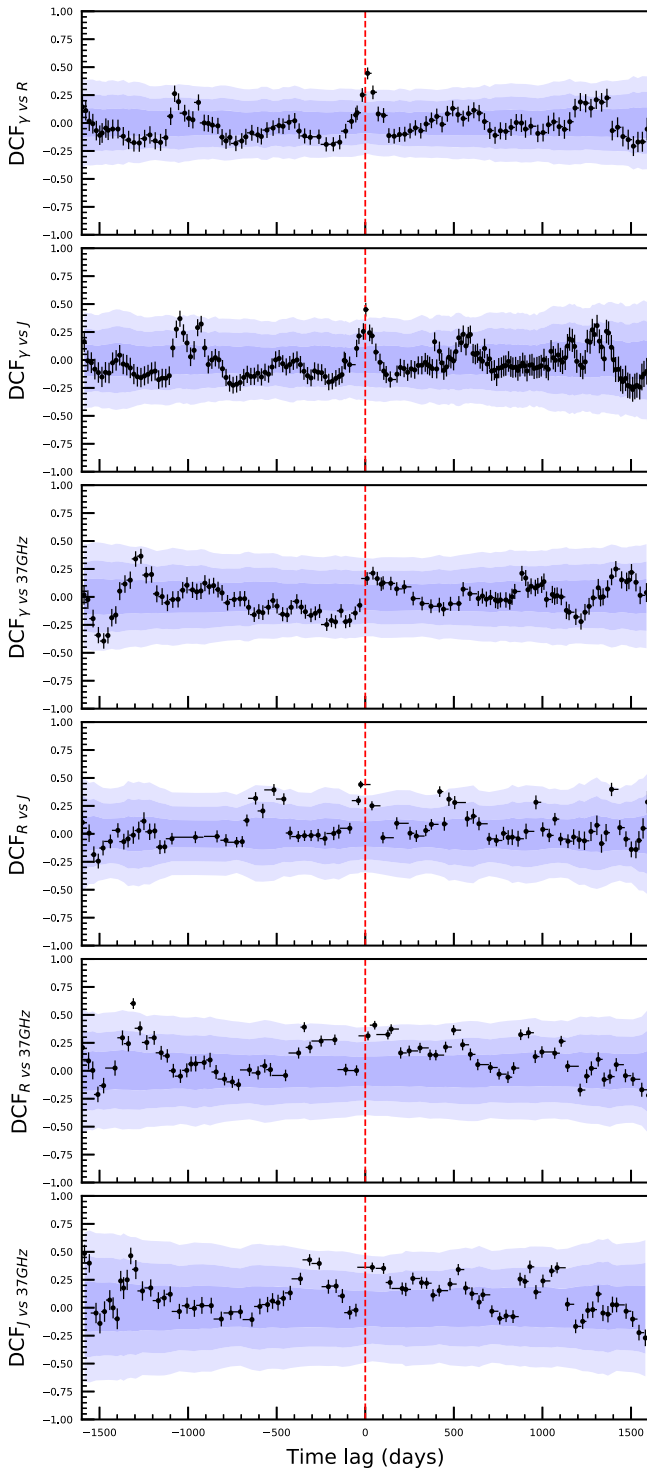
coefficient between these bands and the errors of the time lags corresponding to those peaks are very large. In segment 4, as mentioned above, the radio flares show longer rise and decay timescales than do the changes in the  $\gamma$ -ray and optical/NIR bands. Therefore for this fourth temporal segment, the optical and NIR correlations and broad nominal positive lags to the radio emission that we obtain by applying mathematical methods such as ZDCF are unconvincing.

## 4. QPO Analysis

Over the last 15 yr or so a modest number of QPO detections have been reported in blazars in different EM bands (e.g., Gupta 2014, 2017; Sarkar et al. 2019; Roy et al. 2022a, 2022b; and references therein). PKS 1510–089 is among a few blazars which has had published claims of the detection of QPOs in different EM bands in different temporal spans. In 22 and 37 GHz radio band data taken during 1995–2005, there were indications of QPOs with two periods, P1 = 0.92 yr and P2 = 1.84 yr, where P1 is a harmonic of P2 (Xie et al. 2008). In University of Michigan Radio Astronomical Observatory (UMRAO) data taken at 8 and 14.5 GHz during 1974–2011, indications of multiple QPO periods in the period range 430–1080 days were found (Li et al. 2021). In poorly sampled optical data taken during 1999–2001, a QPO with a period of  $\sim 0.92$  yr was suggested (Xie et al. 2002), though the data stream was not long enough to make this a convincing case. Other poorly sampled NIR K-band and optical R-band light curves of the source taken during the longer span of 2006–2014 apparently displayed multiple periods ranging from 203 to 490 days (Sandrinelli et al. 2016). In the 2006–2014 Fermi-LAT light curve of this blazar, a QPO with a period of  $\sim 115$  days was claimed (Sandrinelli et al. 2016; Castignani et al. 2017). Recently, transient  $\gamma$ -ray QPOs with periods of 3.6 and 92 days in Fermi-LAT data of the source were claimed in two different portions of the light curve (Roy et al. 2022b).

In light of these previous QPO signals from the blazar PKS 1510–089 we now consider for further analysis the independent new data we have presented here: the Metsähovi 37 GHz radio light curve between 2008 and 2018 (plotted in the bottom panel of Figure 1). Modulations indicating a possible quasiperiodic component might be identified by visually inspecting the flux variations with time. We used several methods, the generalized Lomb–Scargle periodogram (GLSP), REDFIT, and the weighted wavelet z-transform (WWZ) to assess the possibility of quasi periodicity in the frequency domain (and also, for WWZ, the time domain). All of these methods can be used for unevenly sampled data which is normally the case for radio light curves observed over the range of few years to decades.





**Figure 4.** ZDCFs between the different wave bands over the entire time of the observations; a ZDCF peak at a positive time lag means LC1 precedes LC2, where the panels are labeled as “LC1” vs. “LC2.” The color contours denote the distribution of random cross-correlations obtained by Monte Carlo simulations; from dark to light these are  $1\sigma$ ,  $2\sigma$ , and  $3\sigma$ .

In this work, we employed the GLSP routine of the PYASTRONOMY<sup>20</sup> package which is based on Zechmeister & Kürster (2009). Figure 6 shows the GLSP plotted against frequency (black curve). The red, blue, and magenta curves

<sup>20</sup> <https://github.com/sczesla/PyAstronomy>

respectively represent  $3\sigma$ ,  $4\sigma$ , and  $5\sigma$  significance levels. The peak of the periodogram is found at a frequency of  $1566_{-184}^{+439}$  days at about  $4\sigma$  nominal significance. But we note that with a data stream that does not exceed 4000 days, this possible period amounts to fewer than three cycles and so can only be considered as a hint at a QPO.

The significance of any peak that could be a QPO is estimated by simulating light curves having properties similar to those of the original light curve. To quantify the significance of a peak it must be assumed that the light curves of blazars can be well represented by the stochastic processes occurring in the accretion disk and the associated jets. For blazars, the PSD over a range of frequencies also can usually be well fit by a PL with a negative spectral index  $\alpha$  (Gupta 2017; Bhatta & Dhital 2020, and references therein). So we use a simple PL as the underlying model for the power spectrum. Any QPO is likely to arise due to coherent disk or jet processes and is different from any stochastic process and thus would appear as a peak in the power spectrum (Ackermann et al. 2012), the significance of which can be assessed. The degree to which any QPO peaks stand above the PL is used to assess the significance of the periodicities (for details, see Tripathi et al. 2021). Wavelet functions are commonly used to examine any evolution in frequency and amplitude of a QPO signal (Torrence & Compo 1998). As the data employed in this work are unevenly sampled, we use an improved version of the wavelet approach, namely the WWZ.

We calculated the WWZ<sup>21</sup> and time-averaged WWZ for the simulated light curves as well as for the actual data, following Tripathi et al. (2021) to calculate the significance levels. If the WWZ amplitude is marginalized over the whole length of the observations, one gets the WWZ as a function of frequency; this is essentially the PSD of the WWZ, which should follow a PL and will be distributed as  $\chi^2$  with two degrees of freedom. Again we use a simple PL as the underlying model to fit the time-averaged WWZ. The left panel of Figure 7 shows a wavelet density plot. Interestingly, there is only a single peak at  $1538_{-23}^{+24}$  days and it is persistent throughout the data stream. The right panel of the Figure 7 plots the time-averaged WWZ against the period. The significance of the highly persistent signal found in the wavelet density plot nominally exceeds  $5\sigma$ .

We also employed the REDFIT method,<sup>22</sup> which essentially compares the data to a first-order autoregressive (AR1) process (Schulz & Mudelsee 2002; Gupta et al. 2018; Hong et al. 2018; and references therein) and calculates significance based on  $\chi^2$  distributions. In AR analyzes, the flux at a given point of time is compared to the data from previous times using a regressive relation and can include any number of such past values. In the simplest AR1 method, only one value previous to the current datum is used to compute the theoretical light curve and subsequently, the AR1 spectrum. For time  $t_i$  ( $i = 1, 2, \dots, N$ ), the AR1 process  $r$  can be written as:

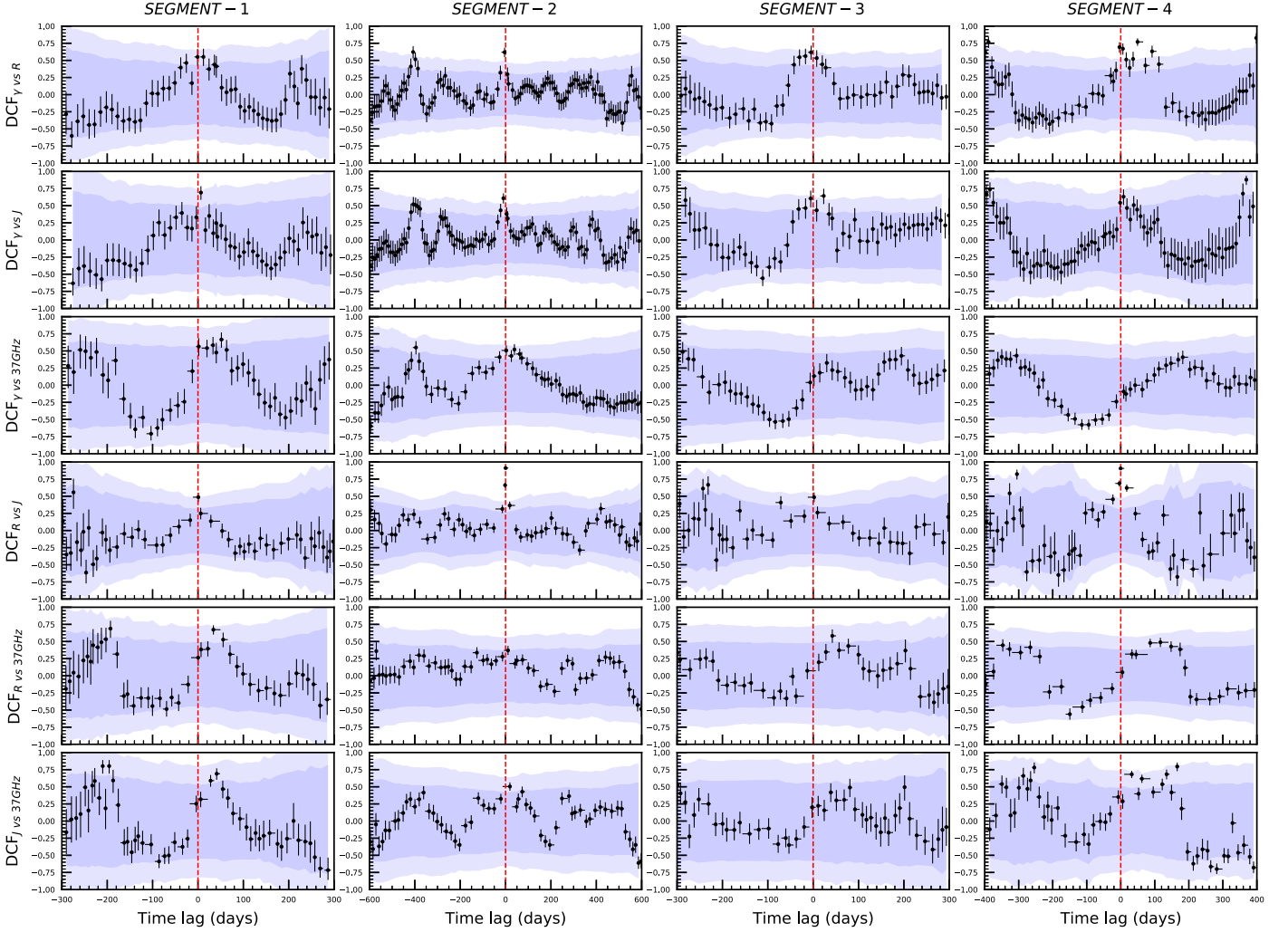
$$r(t_i) = \rho_i r(t_{i-1}) + \epsilon(t_i), \quad (6)$$

$$\rho_i = \exp(-(t_i - t_{i-1})/\tau), \quad (7)$$

<sup>21</sup> <https://www.aavso.org/software-directory>

<sup>22</sup> The code is found at <https://www.marum.de/Prof.-Dr.-michael-schulz/Michael-Schulz-Software.html>.





**Figure 5.** ZDCFs between the different wave bands in the four temporal segments; a ZDCF peak at a positive time lag means LC1 precedes LC2, where the panels are labeled as “LC1” vs. “LC2.” The color contours denote the distribution of random cross-correlations obtained by Monte Carlo simulations; here the dark and light are  $2\sigma$  and  $3\sigma$ , respectively.

where  $\epsilon$  is the Gaussian noise such that the AR1 process has unit variance and zero mean,  $\rho$  denotes the autocorrelation coefficient, and  $\tau$  represents the characteristic timescale for the AR1 process. The power spectrum  $S_{rr}(f_i)$ , corresponding to the AR1 process described in Equation (4) for frequency  $f_i$  up to the Nyquist frequency,  $f_{\text{Nyq}}$  is given as:

$$S_{rr}(f_i) = S_0 \frac{1 - \rho^2}{1 - 2\rho \cos(\pi f_i / f_{\text{Nyq}}) - \rho^2}. \quad (8)$$

The estimated values of  $\rho$  and  $\tau$  for this light curve are found to be 0.92 and 206 days, respectively. Figure 8 plots the normalized REDFIT results against frequency. The solid black and red dashed curves respectively represent the spectrum of the input data and the bias-corrected spectrum. The blue dashed-dotted curve shows the theoretical AR(1) spectrum. The magenta curve represents the  $2\sigma$  confidence curve. The peak around 360 days has a significance exceeding  $2\sigma$  but it is suspiciously close to 1 yr. The otherwise strongest signal is at  $1465^{+56}_{-53}$  days and while it is less than  $2\sigma$  it is consistent with the results from the GLSP and WWZ methods.

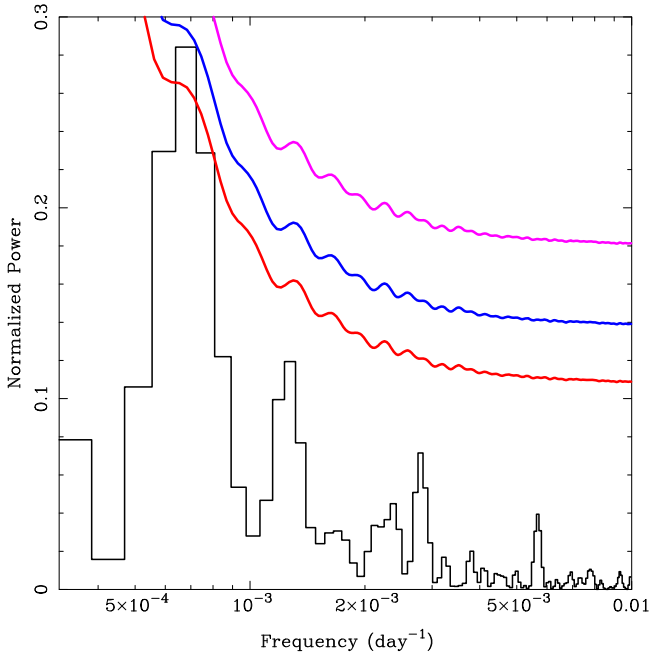
## 5. Discussion

### 5.1. Unveiling the Physics behind the Spectral Variations

Recently, Otero-Santos et al. (2022) used a powerful statistical tool—nonnegative matrix factorization (NMF; see Paatero & Tapper 1994; Ivezić et al. 2014)—to reproduce the spectral variability for some blazars over 10 yr using two to four components. The photometric and spectropolarimetric data used in their study (taken by the Steward Observatory) are partly homologous to the optical  $R$ -band data in this paper, with temporal coverages slightly (by less than a year) longer than ours. This study is critical to understanding the origin of blazar variability. In PKS 1510–089, the spectral variability is explained as the sum of a bright BLR component, a PL component accounting for the nonthermal synchrotron radiation of the relativistic jet, and the blue accretion disk contribution that shows slight variation and lower brightness than the BLR and the PL for the jet. Otero-Santos et al. (2022) concluded that the contribution of the jet component is related to color and showed an RWB trend consistent with our results. For PKS 1510–089, which is a low-synchrotron peaked FSRQ (Ajello et al. 2020) and which has an accretion disk

**Table 4**  
Time Lags, in Days, of the ZDCF Peaks between the Different Bands

Light Curves	ENTIRE TIME	SEGMENT 1	SEGMENT 2	SEGMENT 3	SEGMENT 4
$\gamma$ -rays versus $R$	$13.27^{+22.60}_{-4.40}$	$-0.81^{+2.57}_{-6.85}$	$-4.39^{+2.28}_{-13.72}$	$-4.58^{+2.96}_{-6.52}$	$-3.82^{+4.47}_{-2.52}$
$\gamma$ -rays versus $J$	$2.81^{+16.52}_{-3.17}$	$6.57^{+2.76}_{-4.23}$	$9.85^{+2.24}_{-6.94}$	$-5.42^{+3.79}_{-5.01}$	$8.13^{+4.47}_{-2.52}$
$\gamma$ -rays versus 37 GHz	...	$51.65^{+5.24}_{-3.65}$	$39.03^{+3.77}_{-5.79}$	...	...
$R$ versus $J$	$-25.97^{+55.87}_{-8.08}$	$0.81^{+2.17}_{-11.81}$	$0.16^{+11.78}_{-0.16}$	$2.05^{+3.75}_{-14.01}$	$-0.42^{+10.52}_{-1.53}$
$R$ versus 37 GHz	$53.5^{+5.96}_{-28.02}$	$34.01^{+15.63}_{-3.48}$	$10.89^{+3.00}_{-18.07}$	$42.20^{+8.25}_{-2.58}$	...
$J$ versus 37 GHz	$39.64^{+16.01}_{-84.76}$	$41.25^{+7.56}_{-2.43}$	$19.18^{+6.55}_{-32.35}$	$38.84^{+4.91}_{-3.12}$	...



**Figure 6.** GLSP of the radio light curve of PKS 1510–089 for the duration 2008–2018. The black histogram denotes the normalized GLSP. The solid red, blue, and magenta curves denote  $3\sigma$ ,  $4\sigma$ , and  $5\sigma$  confidence intervals, respectively.

temperature estimated as 40,000 K (Abdo et al. 2010), the synchrotron peak and the thermal accretion disk spectrum peak are located in the NIR and the far-UV, respectively. We note that the thermal disk spectrum is bluer, especially in this source, where the accretion disk temperature is very high. However, nonthermal photons have a redder spectral shape. So, the observed colors are influenced by changes in accretion disk emission, jet emission, or both. It is reasonable to expect that we would observe a bluer-when-brighter trend in the low-flux regime if thermal radiation from optical/NIR wavelengths is much stronger than or even swamps the jet radiation. However, our investigation finds the opposite RWB trend. We can infer that the Doppler-boosted jet emission dominates the entire radiation process, even the optical band. Moreover, in the optical/NIR high-flux state, RWB behavior is also displayed throughout the observation period. So we also can infer that the high-flux states of optical/NIR emission come from enhanced jet activity, and increased nonthermal emission results in a reddening of the color.

### 5.2. Multiband Cross-correlation Analysis

Blazars are the most powerful, persistent extragalactic broadband sources. The region responsible for the broadband

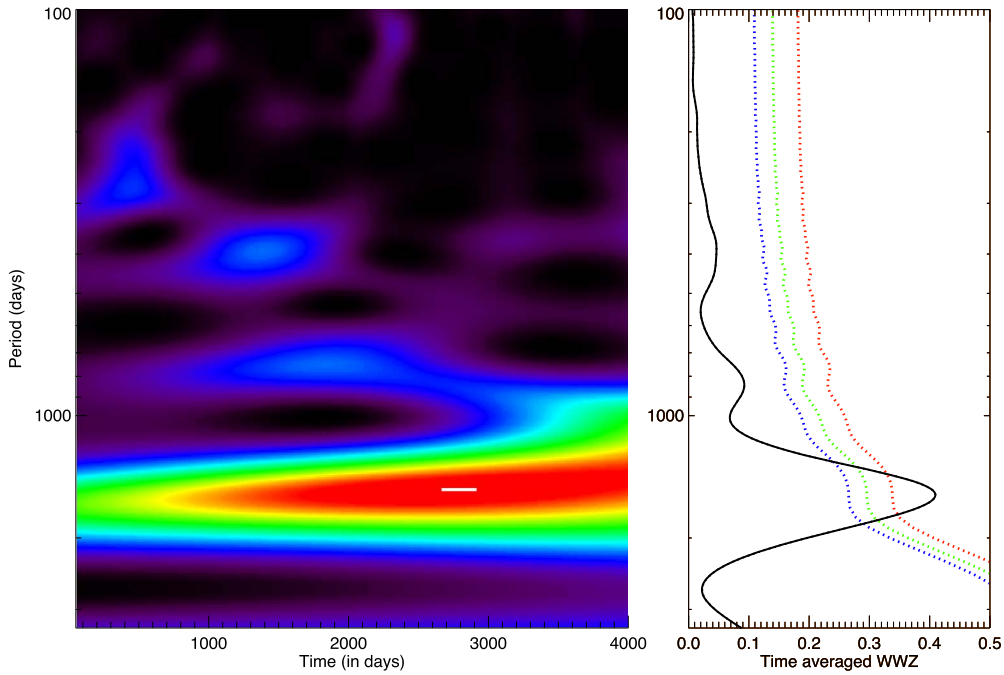
emission is highly compact—beyond the resolution limit of modern facilities even for the nearest sources, e.g., M87 and Sgr A\* (Event Horizon Telescope Collaboration et al. 2019a, 2019b, 2022). However, the jet region is optically thin at NIR and higher energies and thus, temporal flux variability allows us to access the spatial extent buried under the resolution limit and is currently the only way to infer these spatial scales. Further, though rapid and strong flux variability is one of the defining characteristics of blazars, these high states are rarely accompanied by the strong spectral changes that would indicate a departure from its SED class.

#### 5.2.1. $\gamma$ -Rays versus Optical/NIR

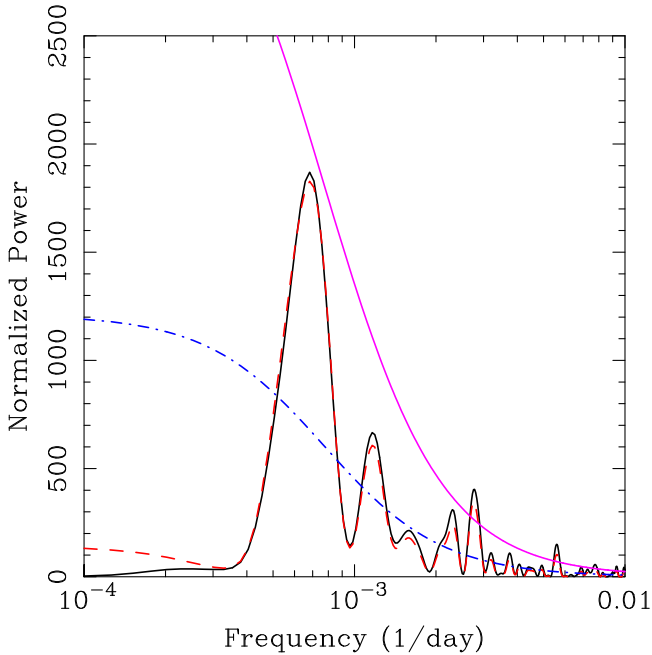
The notable correlation between the  $\gamma$ -ray and optical/NIR emissions indicates simultaneous variations (within the sampling intervals) and thus strongly supports the leptonic model. Ramakrishnan et al. (2016) studied 15 blazars and reported two sources with a strong correlation in optical and  $\gamma$ -ray emissions with zero time delay, one of which is PKS 1510–089. We validated these previous results using high-quality data over a more extended period. In the leptonic scenario, the high-energy emission is produced by relativistic electrons scattering seed photons from low energy to high energy through the IC process. Studies employing SED modeling of PKS 1510–089 show that synchrotron radiation from relativistic electrons can adequately describe the millimeter to optical emissions, while high-energy emissions (X-rays to  $\gamma$ -rays) cannot. These previous studies have shown that X-ray and  $\gamma$ -ray emissions are also an EC process of the BLR and DT photons (Kataoka et al. 2008; Abdo et al. 2010; Brown 2013; Barnacka et al. 2014; Prince et al. 2019). Moreover, Prince et al. (2019) inferred that the  $\gamma$ -ray and optical emissions are produced in the same region from the flux doubling times of their  $\gamma$ -ray, optical, and UV light curves.

#### 5.2.2. Optical versus NIR

As stated above, the synchrotron radiation of the relativistic jet is the primary source of its optical and NIR radiation (e.g., Blandford & Rees 1978). However, additional contributions are expected from thermal radiation from the accretion disk and torus. A statistical study suggests that the host galaxy and BLR may also contribute significantly to the optical band (Otero-Santos et al. 2022). Quantifying all possible optical and NIR emission contributions has been a challenge. The combination of the color trend and correlation analysis of optical and NIR light curves is an effective way to understand the radiation mechanism of this source. We determined that the jet emission dominates the optical and NIR color variability behavior throughout the observation period.



**Figure 7.** Wavelet result for the 2008–2018 light curve. Left panel: WWZ plot with red denoting the maximum wavelet power which decreases toward violet and black. Right panel: time-averaged WWZ (solid black curve); the blue, green, and red dotted curves represent  $3\sigma$ ,  $4\sigma$ , and  $5\sigma$  confidence intervals, respectively.



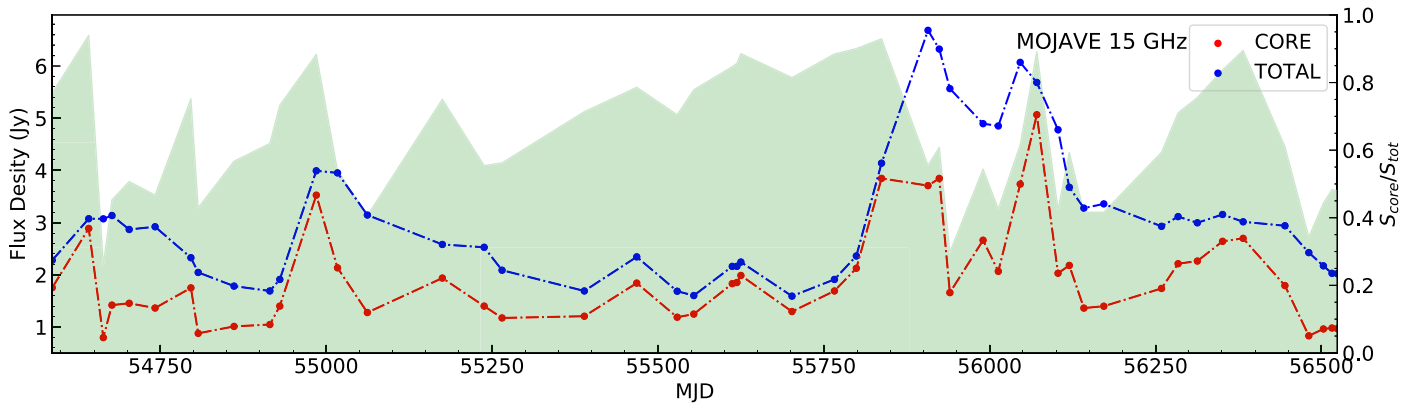
**Figure 8.** REDFIT result for the 2008–2018 light curve. The black solid curve and the red dashed curve represent the spectrum of input data and the bias-corrected spectrum, respectively. The blue dashed-dotted curve denotes the AR(1) theoretical spectrum and the solid magenta curve is the 95% confidence curve.

The correlation between the optical  $B$ -band and NIR  $J$ -band observation data of the SMARTS monitoring program from 2008 to 2010 was studied at an early stage (Bonning et al. 2012). We use the  $R$ -band data released by this program and supplementary data from the Steward Observatory to revisit the correlation between the optical and NIR emissions with longer observation times and denser sampling intervals. We confirm the results of Bonning et al. (2012) that there is a very good

correlation between the light curves from the optical and NIR bands. Significant correlations with zero time lag are seen between the optical  $R$ -band and NIR  $J$ -band light curves, indicating that the bulk of these emissions are simultaneous or that any time lag occurs on a timescale smaller than the observational cadence. It can further be inferred that the main emission region of the optical and NIR photons is cospatial and originates in the jet.

### 5.2.3. $\gamma$ -Ray versus Radio

Several studies have reported a time delay between the  $\gamma$ -ray emission and the radio emission measured by both a single radio dish and VLBI. For single-dish data,  $\gamma$ -ray flares occur earlier than radio flares (Fuhrmann et al. 2014; Max-Moerbeck et al. 2014a). And for VLBI data, Pushkarev et al. (2010) used a large sample of 183 bright Fermi-detected sources and found that the correlations were strong between the  $\gamma$ -ray emission and the VLBA core-component emission with the  $\gamma$ -ray emission preceding the radio emission. Recently, they performed a correlation analysis for a larger sample that had been accumulated and found the time delay is in good agreement with their previous results (Kramarenko et al. 2022). The light curve obtained from single-dish observations or VLBA observations yielded similar results when correlated with the  $\gamma$ -ray light curve. The above results are supported for two reasons. First, the radio core dominates the radio emission, which makes the core flux density and total flux density light curves’ characteristics similar in terms of VLBA observations. Second, the parsec-scale emission region dominates the radio flux density variations, which reflect that the characteristics of the total light curves obtained by single-dish observations and VLBA observations are similar. Similar characteristics refer to the flares occurring almost quasi-simultaneously, with roughly the same upward and downward trends, although the above characteristics vary from source to source.



**Figure 9.** Archived 15 GHz VLBI data light curves for PKS 1510–089. Red circles represent the fitted core features flux density from Angelakis et al. (2019), and blue circles represent the VLBI total flux density from the MOJAVE web page <https://www.cv.nrao.edu/MOJAVE/sourcepages/1510-089.shtml> (Lister et al. 2018). The values that make up the upper border of the green shade represent the ratio of the core flux density to the total flux density for each epoch.

We can compare the magnitudes of the core and total flux densities of PKS 1510–089 at multiple epochs when 15 GHz VLBI observations were made by collecting data released by the MOJAVE program (see Figure 9). Here we also calculate the values ( $S_{\text{core}}/S_{\text{VLBA}}$ ) that characterize the core dominance degree of each epoch (also see Figure 9), where  $S_{\text{core}}$  and  $S_{\text{VLBA}}$  are the core and total flux density, respectively. It can be clearly seen that this source is core dominated. In addition, for PKS 1510–089, it has been demonstrated that the parsec-scale emission region dominates the radio flux density variability (Oriente et al. 2013). So, the above  $S_{\text{core}}$  and  $S_{\text{VLBA}}$  variations are not much different from the radio emission measured by a single antenna. We therefore can reasonably predict that if there were even more densely sampled VLBI data sets available we would obtain  $\gamma$ -ray and radio radiation correlations that are consistent with single-dish data analyses. We should remember that intensive monitoring is essential to understand the correlation between the cross-band activity of the long-term trends, so our choice of the well-sampled 37 GHz single-dish data to perform the correlation analysis is sensible.

In the classical and commonly used shock-in-jet model (e.g., Marscher & Gear 1985; Türler et al. 2000; Fromm et al. 2011), the shock propagates down a conical jet and accelerates the relativistic particles at the shock front. These particles propagate behind the shock front and lose their energy through different energy-loss mechanisms, such as adiabatic expansion and synchrotron radiation. The most widely accepted view is that the moving shock is an intrinsic factor responsible for the observed radio flux density variations.

As mentioned above, the current investigation found that the  $\gamma$ -ray emission precedes the radio emission. Several studies have attempted to interpret this result, suggesting that  $\gamma$ -ray luminosity variations may be connected to the same shocked radio features and connect these two frequency emissions through the shock (Fuhrmann et al. 2014; Ramakrishnan et al. 2015). Suppose radio and  $\gamma$ -ray emissions are triggered by shocks propagating in the relativistic jet. In this scenario, the time lag is related to the distance between the radio core and the location where the  $\gamma$ -ray emission is produced. This can also be understood as an unresolved core centroid moving toward the position of the black hole as the observing frequency increases (Blandford & Königl 1979; Königl 1981), i.e., the so-called “core shift” effect. The  $\gamma$ -ray photons escape from the jet immediately when the shock arrives, and it takes a while for the shock (perturbation) to propagate farther along the jet until

it reaches the  $\tau = 1$  surface from which radio photons at the specified radio frequency can escape.

In our study, we also found that the  $\gamma$ -ray emission leads the radio emission in segment 1 and segment 2. Moreover, as shown above, the flux density variability of PKS 1510–089 is dominated by the flux density of the core fitted in the VLBI images. Hence, a possible explanation for these results may be the above scenario involving a shock. We estimate the separation of the  $\gamma$ -ray and the 37 GHz emission regions following the method and assumptions of Pushkarev et al. (2010):

$$\Delta r = r_{\gamma} - r_{\text{Radio}} = \frac{\delta\Gamma\beta c\Delta t_{\text{Radio}-\gamma}^{\text{obs}}}{1+z} = \frac{\beta_{\text{app}}c\Delta t_{\text{Radio}-\gamma}^{\text{obs}}}{(1+z)\sin\theta}, \quad (9)$$

where  $\beta_{\text{app}}$  is the apparent speed,  $z$  is the redshift,  $\theta$  is the viewing angle, and  $\Delta t_{\text{Radio}-\gamma}^{\text{obs}}$  is the time lag in the observer’s frame. Using  $\beta_{\text{app}} = 28$  (Lister et al. 2021),  $\theta = 2^{\circ}5$  (Homan et al. 2021), and  $\Delta t_{\text{Radio}-\gamma}^{\text{obs}} = 45$  days, which is the average of the time lags of the two segments with significant correlation, the distance between the two emission regions is estimated as 17.82 pc, and the corresponding projected distance is 0.78 pc.

From the core shift measure ( $\Omega$ ; defined in Lobanov 1998) for PKS 1510–089 by Pushkarev et al. (2012), we can estimate the distance between the radio core and the true jet apex as 8.36 pc. So, the value of the distance between the  $\gamma$ -ray emission region and the jet apex is a negative value. The above results are in agreement with Kramarenko et al. (2022)’s findings, who calculated the radio emission lagged the  $\gamma$ -ray emission by  $111_{-30}^{+16}$  days in the observer’s frame and the  $\gamma$ -ray emission generation region is  $-12.00_{-8.65}^{+13.71}$  pc from the central engine. The jet is widely thought to be launched in the vicinity of the supermassive black hole (SMBH) within  $100 R_s$  (Schwarzschild radius; Meier et al. 2001). Referring to previous studies, the black hole mass of PKS 1510–089 is estimated to be on the order of  $10^7$ – $10^8 M_{\odot}$  (Oshlack et al. 2002; Xie et al. 2005; Liu et al. 2006; Abdo et al. 2010; Castignani et al. 2017; Park & Trippie 2017; Rakshit 2020). Therefore, the jet apex is  $10^{-5}$ – $10^{-6}$  pc away from the central engine or SMBH, which is negligible. The negative value of the distance from the location of the  $\gamma$ -ray emission production to the central engine might further suggest that the conjecture that the perturbation propagates in a straight jet geometry is too simple; Kramarenko et al. (2022) offer several alternative interpretations.



### 5.2.4. Optical/NIR versus Radio

For this source, as discussed above, the optical and NIR emissions are dominated by nonthermal synchrotron emission from the relativistic jet and their emission region is almost cospatial. We see that the optical and radio ZDCF profiles are very similar to the NIR and radio ZDCF profiles, while the lack of some *J*-band data near MJD 57500 compared to the *R*-band data results in some visible differences between their profiles in segment 4. Meanwhile, due to the seasonal gap in the data of this particular segment, we cannot arrive at a firm conclusion about the correlation results in this segment. However, the remaining three segments show that the radio is lagging the optical/NIR radiation. These results are in agreement with the above model; in other words, the scenario in which the radio emission lags behind optical/NIR emission is analogous to the scenario in which the  $\gamma$ -ray emission lags behind the radio emission. Although no firm conclusions have been drawn to date on the correlations between the optical/NIR and radio emissions for blazars in general, correlation analyses between optical/NIR and radio bands in large samples or individual sources have revealed radio emission lagging the optical/NIR in a substantial fraction of cases (e.g., Zhang et al. 2017; Sarkar et al. 2019).

### 5.3. QPO Analysis

We found a hint of a possible QPO of about 1580 days in the 37 GHz radio emission, but it might only be confirmed through even longer future studies. Since the radio emission is synchrotron emission from the jet, jet precession seems a potential interpretation of such a lengthy putative QPO. However, almost the entire multiband emission is from the jet and thus, similar temporal profiles are expected across the entire EM bands unless there is a strong spectral change, which does not seem to be the case here. Though the radio emission correlates very well with the emission in the other bands, the temporal profile is very different, with much smoother and broader peaks. Also, a large fraction of the radio photons often come from the unresolved core, as in the present case (see Figure 9).

## 6. Summary

In this study, we performed a correlation analysis of the multiband light curves of the FSRQ PKS 1510–089, in  $\gamma$ -ray, optical, NIR, and 37 GHz radio band data sets spanning around 10 yr (2008 February to 2017 September). The  $\gamma$ -ray data come from LAT on board the space-based Fermi Gamma-ray Space Telescope, the optical *R*-band data and NIR *J*-band data are from the public archive of the SMARTS and the Steward Observatory telescopes, and the radio observations at 37 GHz were made at the 14 m radio telescope at the Metsähovi Radio Observatory of Aalto University. We also employed several methods to search for the QPO phenomenon in the radio light curve between 2008 and 2018. Through a series of analyses, we obtain the following results:

1. This source shows RWB behavior whether compared during individual segments or grouped by brightness states, indicating that jet emission dominates accretion disk emission throughout the observation period, even in low-flux states.

2. All segments show strong  $\gamma$ -ray and optical/NIR correlations, and the correlation between  $\gamma$ -rays and radio is shown in the first two segments with a nonzero time lag. The existence of these correlations lends support to the leptonic model of  $\gamma$ -ray emission. For PKS 1510–089, the nominal distance from the location of the  $\gamma$ -ray emission production to the central engine is a negative value, found using a simple model of shock propagating down a conical jet. This could indicate that the morphology of the conical jet may have been altered by jet dynamics, making the model unable to support such a complex situation.
3. The correlation analysis reveals a clear, and unsurprising, correlation between the optical *R*-band and NIR *J*-band emissions, implying that these flares are simultaneous, or at least that the time lag between these light curves is shorter than the cadence of the observations. Additionally, the optical and NIR flares are caused mainly by synchrotron radiation from the jet, and their emission regions are almost cospatial.
4. We confirm that variations in the optical/NIR bands lead to variations in the 37 GHz radio band, and these results again suggest that the origin of the radiation that dominates these three frequencies is the same. This correlation indirectly indicates that other components, such as thermal radiation, make lesser contributions to the total optical and NIR fluxes. This conclusion of jet dominance is further supported by the color index changes in the optical and NIR bands.
5. A nominal QPO signal is found in the radio light curve, but the period of  $\sim 1580$  days is too long compared to the length of the observations to be trusted.

This publication makes use of data obtained at Metsähovi Radio Observatory, operated by Aalto University in Finland. The various diligent observers of Aalto University in Finland are thankfully acknowledged. This paper has made use of up-to-date SMARTS optical/near-infrared light curves that are available at [www.astro.yale.edu/smarts/glast/home.php](http://www.astro.yale.edu/smarts/glast/home.php). SMARTS observations of Large Area Telescope-monitored blazars are supported by Yale University and Fermi GI grant NNX 12AP15G, and the SMARTS 1.3 m observing queue received support from NSF grant AST-0707627. Data from the Steward Observatory spectropolarimetric monitoring project were used. This program is supported by Fermi GI grants NNX08AW56G, NNX09AU10G, NNX12AO93G, and NNX15AU81G. This work has made use of publicly available Fermi-LAT data obtained from FSSC's website data server and provided by NASA Goddard Space Flight Center. This research has made use of data from the MOJAVE database that is maintained by the MOJAVE team (Lister et al. 2018).




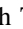

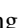


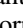
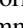
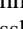





### Acknowledgments

This work is supported by the National Key R&D Intergovernmental Cooperation Program of China (2023YFE0102300, 2022YFE0133700), the Regional Collaborative Innovation Project of Xinjiang Uyghur Autonomous Region (2022E01013), the National Natural Science Foundation of China (12173078, 11773062), and the Chinese Academy of Sciences (CAS) “Light of West China” Program (2017-XBQNXZ-A-008, 2021-XBQNXZ-005). P.K. acknowledges support from the Department of Science and Technology (DST), government of India, through the DST-INSPIRE Faculty

grant (DST/INSPIRE/04/2020/002586). A.C.G. is partially supported by the Chinese Academy of Sciences (CAS) President's International Fellowship Initiative (PIFI; grant No. 2016VMB073). The work of A.T. was supported by the Innovation Program of the Shanghai Municipal Education Commission, grant No. 2019-01-07-00-07-E00035, and the National Natural Science Foundation of China (NSFC), grant No. 11973019. M.F.G. acknowledges support from the National Natural Science Foundation of China (grant No. 11873073), Shanghai Pilot Program for Basic Research Chinese Academy of Science, Shanghai Branch (JCYJ-SHFY2021-013), and the science research grants from the China Manned Space Project (No. CMSCSST-2021-A06).

*Software:* Python.

## ORCID iDs

Q. Yuan  <https://orcid.org/0000-0003-4671-1740>  
 Pankaj Kushwaha  <https://orcid.org/0000-0001-6890-2236>  
 Alok C. Gupta  <https://orcid.org/0000-0002-9331-4388>  
 Ashutosh Tripathi  <https://orcid.org/0000-0002-3960-5870>  
 Paul J. Wiita  <https://orcid.org/0000-0002-1029-3746>  
 M. Zhang  <https://orcid.org/0000-0002-8315-2848>  
 X. Liu  <https://orcid.org/0000-0001-9815-2579>  
 Anne Lähteenmäki  <https://orcid.org/0000-0002-0393-0647>  
 Merja Tornikoski  <https://orcid.org/0000-0003-1249-6026>  
 Joni Tammi  <https://orcid.org/0000-0002-9164-2695>  
 Venkatesh Ramakrishnan  <https://orcid.org/0000-0002-9248-086X>  
 L. Cui  <https://orcid.org/0000-0003-0721-5509>  
 X. Wang  <https://orcid.org/0000-0001-8221-9601>  
 M. F. Gu  <https://orcid.org/0000-0002-4455-6946>  
 Cosimo Bambi  <https://orcid.org/0000-0002-3180-9502>  
 A. E. Volvach  <https://orcid.org/0000-0002-3839-3466>

## References

- Abdo, A. A., Ackermann, M., Agudo, I., et al. 2010, *ApJ*, 721, 1425  
 Abdullahi, S., Acero, F., Ackermann, M., et al. 2020, *ApJS*, 247, 33  
 Acharyya, A., Chadwick, P. M., & Brown, A. M. 2021, *MNRAS*, 500, 5297  
 Ackermann, M., Ajello, M., Ballet, J., et al. 2012, *ApJ*, 751, 159  
 Aharonian, F., Akhperjanian, A., Beilicke, M., et al. 2002, *A&A*, 393, 89  
 Aharonian, F., Akhperjanian, A. G., Anton, G., et al. 2009, *A&A*, 502, 749  
 Aharonian, F., Akhperjanian, A. G., Aye, K. M., et al. 2005a, *A&A*, 430, 865  
 Aharonian, F., Akhperjanian, A. G., Bazer-Bachi, A. R., et al. 2005b, *A&A*, 442, 895  
 Aharonian, F., Akhperjanian, A. G., Bazer-Bachi, A. R., et al. 2007, *ApJL*, 664, L71  
 Ahnen, M. L., Ansoldi, S., Antonelli, L. A., et al. 2017, *A&A*, 603, A29  
 Ajello, M., Angioni, R., Axelsson, M., et al. 2020, *ApJ*, 892, 105  
 Aleksić, J., Ansoldi, S., Antonelli, L. A., et al. 2014, *A&A*, 569, A46  
 Alexander, T. 2013, arXiv:1302.1508  
 Alexander, T. 1997, in *Astronomical Time Series*, ed. D. Maoz, A. Sternberg, & E. M. Leibowitz (Dordrecht: Kluwer), 163  
 Angelakis, E., Fuhrmann, L., Myserlis, I., et al. 2019, *A&A*, 626, A60  
 Arsioli, B., & Chang, Y. L. 2018, *A&A*, 616, A63  
 Barnacka, A., Moderski, R., Behera, B., Brun, P., & Wagner, S. 2014, *A&A*, 567, A113  
 Beaklini, P. P. B., Dominici, T. P., & Abraham, Z. 2017, *A&A*, 606, A87  
 Bhatta, G., & Dhital, N. 2020, *ApJ*, 891, 120  
 Błażewski, M., Blaylock, G., Bond, I. H., et al. 2005, *ApJ*, 630, 130  
 Blandford, R. D., & Königl, A. 1979, *ApJ*, 232, 34  
 Blandford, R. D., & Rees, M. J. 1978, in *Pittsburgh Conf. on BL Lac Objects*, ed. A. M. Wolfe, 328  
 Bonning, E., Urry, C. M., Bailyn, C., et al. 2012, *ApJ*, 756, 13  
 Böttcher, M. 2019, *Galax*, 7, 20  
 Böttcher, M., Reimer, A., Sweeney, K., & Prakash, A. 2013, *ApJ*, 768, 54  
 Brown, A. M. 2013, *MNRAS*, 431, 824  
 Buxton, M. M., Bailyn, C. D., Capelo, H. L., et al. 2012, *AJ*, 143, 130  
 Castignani, G., Pian, E., Belloni, T. M., et al. 2017, *A&A*, 601, A30  
 Chen, X., Fossati, G., Böttcher, M., & Liang, E. 2012, *MNRAS*, 424, 789  
 Connolly, S. D. 2015, arXiv:1503.06676  
 Costamante, L., Cutini, S., Tosti, G., Antolini, E., & Tramacere, A. 2018, *MNRAS*, 477, 4749  
 Edelson, R. A., & Krolik, J. H. 1988, *ApJ*, 333, 646  
 Emmanoulopoulos, D., McHardy, I. M., & Papadakis, I. E. 2013, *MNRAS*, 433, 907  
 Event Horizon Telescope Collaboration, Akiyama, K., Alberdi, A., et al. 2019a, *ApJL*, 875, L2  
 Event Horizon Telescope Collaboration, Akiyama, K., Alberdi, A., et al. 2019b, *ApJL*, 875, L4  
 Event Horizon Telescope Collaboration, Akiyama, K., Alberdi, A., et al. 2022, *ApJL*, 930, L15  
 Fernandes, S., Patiño-Álvarez, V. M., Chavushyan, V., Schlegel, E. M., & Valdés, J. R. 2020, *MNRAS*, 497, 2066  
 Fossati, G., Buckley, J. H., Bond, I. H., et al. 2008, *ApJ*, 677, 906  
 Fromm, C. M., Perucho, M., Ros, E., et al. 2011, *A&A*, 531, A95  
 Fuhrmann, L., Angelakis, E., Zensus, J. A., et al. 2016, *A&A*, 596, A45  
 Fuhrmann, L., Larsson, S., Chiang, J., et al. 2014, *MNRAS*, 441, 1899  
 Gaur, H., Gupta, A. C., Wiita, P. J., et al. 2014, *ApJL*, 781, L4  
 Gupta, A. C. 2014, *JApA*, 35, 307  
 Gupta, A. C. 2017, *Galax*, 6, 1  
 Gupta, A. C., Gaur, H., Wiita, P. J., et al. 2019, *AJ*, 157, 95  
 Gupta, A. C., Kushwaha, P., Carrasco, L., et al. 2022, *ApJS*, 260, 39  
 Gupta, A. C., Mangalam, A., Wiita, P. J., et al. 2017, *MNRAS*, 472, 788  
 Gupta, A. C., Tripathi, A., Wiita, P. J., et al. 2018, *A&A*, 616, L6  
 H.E.S.S. Collaboration, Abramowski, A., Acero, F., et al. 2013, *A&A*, 554, A107  
 Hodgson, J. A., Krichbaum, T. P., Marscher, A. P., et al. 2017, *A&A*, 597, A80  
 Homan, D. C., Cohen, M. H., Hovatta, T., et al. 2021, *ApJ*, 923, 67  
 Hong, S., Xiong, D., & Bai, J. 2018, *AJ*, 155, 31  
 Horan, D., Acciari, V. A., Bradbury, S. M., et al. 2009, *ApJ*, 695, 596  
 Isler, J. C., Urry, C. M., Coppi, P., et al. 2017, *ApJ*, 844, 107  
 Ivezić, Ž., Connelly, A. J., VanderPlas, J. T., & Gray, A. 2014, *Statistics, Data Mining, and Machine Learning in Astronomy* (1st ed.; Princeton, NJ: Princeton Univ. Press)  
 Jorstad, S., & Marscher, A. 2016, *Galax*, 4, 47  
 Jorstad, S. G., Marscher, A. P., Morozova, D. A., et al. 2017, *ApJ*, 846, 98  
 Kataoka, J., Madejski, G., Sikora, M., et al. 2008, *ApJ*, 672, 787  
 Katarzyński, K., Sol, H., & Kus, A. 2001, *A&A*, 367, 809  
 Kellermann, K. I., Vermeulen, R. C., Zensus, J. A., & Cohen, M. H. 1998, *AJ*, 115, 1295  
 Kendall, M., & Stuart, A. 1973, *The Advanced Theory of Statistics* (3rd edn.; London: Charles Griffin)  
 Kendall, M. G., & Stuart, A. 1969, *The Advanced Theory of Statistics*, Vol. 1 (London: Charles Griffin)  
 Konigl, A. 1981, *ApJ*, 243, 700  
 Kramarenko, I. G., Pushkarev, A. B., Kovalev, Y. Y., et al. 2022, *MNRAS*, 510, 469  
 Krawczynski, H., Sambruna, R., Kohnle, A., et al. 2001, *ApJ*, 559, 187  
 Kushwaha, P., Chandra, S., Misra, R., et al. 2016, *ApJL*, 822, L13  
 Kushwaha, P., Gupta, A. C., Misra, R., & Singh, K. P. 2017a, *MNRAS*, 464, 2046  
 Kushwaha, P., Gupta, A. C., Wiita, P. J., et al. 2018a, *MNRAS*, 473, 1145  
 Kushwaha, P., Gupta, A. C., Wiita, P. J., et al. 2018b, *MNRAS*, 479, 1672  
 Kushwaha, P., Sahayanathan, S., & Singh, K. P. 2013, *MNRAS*, 433, 2380  
 Kushwaha, P., Sinha, A., Misra, R., Singh, K. P., & de Gouveia Dal Pino, E. M. 2017b, *ApJ*, 849, 138  
 Li, X.-P., Zhao, L., Yan, Y., et al. 2021, *JApA*, 42, 92  
 Lira, P., Arévalo, P., Uttley, P., McHardy, I., & Breedt, E. 2011, *MNRAS*, 415, 1290  
 Lister, M. L., Aller, M. F., Aller, H. D., et al. 2018, *ApJS*, 234, 12  
 Lister, M. L., Homan, D. C., Kellermann, K. I., et al. 2021, *ApJ*, 923, 30  
 Liu, Y., Jiang, D. R., & Gu, M. F. 2006, *ApJ*, 637, 669  
 Lobanov, A. P. 1998, *A&A*, 330, 79  
 MAGIC Collaboration, Acciari, V. A., Ansoldi, S., et al. 2018, *A&A*, 619, A159  
 Mannheim, K., & Biermann, P. L. 1992, *A&A*, 253, L21  
 Marscher, A. P., & Gear, W. K. 1985, *ApJ*, 298, 114  
 Marscher, A. P., Jorstad, S. G., Larionov, V. M., et al. 2010, *ApJL*, 710, L126  
 Max-Moerbeck, W., Hovatta, T., Richards, J. L., et al. 2014a, *MNRAS*, 445, 428  
 Max-Moerbeck, W., Richards, J. L., Hovatta, T., et al. 2014b, *MNRAS*, 445, 437  
 Meier, D. L., Koide, S., & Uchida, Y. 2001, *Sci*, 291, 84

- Meyer, M., Scargle, J. D., & Blandford, R. D. 2019, *ApJ*, **877**, 39
- Mücke, A., & Protheroe, R. J. 2001, *Aph*, **15**, 121
- Orienti, M., Koyama, S., D'Ammando, F., et al. 2013, *MNRAS*, **428**, 2418
- Oshlack, A. Y. K. N., Webster, R. L., & Whiting, M. T. 2002, *ApJ*, **576**, 81
- Otero-Santos, J., Acosta-Pulido, J. A., Becerra González, J., et al. 2022, *MNRAS*, **511**, 5611
- Paatero, P., & Tapper, U. 1994, *Environmetrics*, **5**, 111
- Park, J., & Trippe, S. 2017, *ApJ*, **834**, 157
- Petry, D., Böttcher, M., Connaughton, V., et al. 2000, *ApJ*, **536**, 742
- Prince, R., Gupta, N., & Nalewajko, K. 2019, *ApJ*, **883**, 137
- Pushkarev, A. B., Hovatta, T., Kovalev, Y. Y., et al. 2012, *A&A*, **545**, A113
- Pushkarev, A. B., Kovalev, Y. Y., & Lister, M. L. 2010, *ApJL*, **722**, L7
- Rakshit, S. 2020, *A&A*, **642**, A59
- Ramakrishnan, V., Hovatta, T., Nieppola, E., et al. 2015, *MNRAS*, **452**, 1280
- Ramakrishnan, V., Hovatta, T., Tornikoski, M., et al. 2016, *MNRAS*, **456**, 171
- Rebillot, P. F., Badran, H. M., Blaylock, G., et al. 2006, *ApJ*, **641**, 740
- Richards, J. L., Max-Moerbeck, W., Pavlidou, V., et al. 2011, *ApJS*, **194**, 29
- Roy, A., Chitnis, V. R., Gupta, A. C., et al. 2022a, *MNRAS*, **513**, 5238
- Roy, A., Sarkar, A., Chatterjee, A., et al. 2022b, *MNRAS*, **510**, 3641
- Sandrinelli, A., Covino, S., Dotti, M., & Treves, A. 2016, *AJ*, **151**, 54
- Sarkar, A., Chitnis, V. R., Gupta, A. C., et al. 2019, *ApJ*, **887**, 185
- Schlafly, E. F., & Finkbeiner, D. P. 2011, *ApJ*, **737**, 103
- Schlegel, D. J., Finkbeiner, D. P., & Davis, M. 1998, *ApJ*, **500**, 525
- Schulz, M., & Mudelsee, M. 2002, *Computers Geosciences*, **28**, 421
- Smith, P. S., Montiel, E., Rightley, S., et al. 2009, arXiv:0912.3621
- Tanner, A. M., Bechtold, J., Walker, C. E., Black, J. H., & Cutri, R. M. 1996, *AJ*, **112**, 62
- Tavecchio, F., Maraschi, L., Sambruna, R. M., & Urry, C. M. 2000, *ApJL*, **544**, L23
- Teraesranta, H., Tornikoski, M., Mujunen, A., et al. 1998, *A&AS*, **132**, 305
- Thompson, D. J., Djorgovski, S., & de Carvalho, R. 1990, *PASP*, **102**, 1235
- Torrence, C., & Compo, G. P. 1998, *BAMS*, **79**, 61
- Tripathi, A., Gupta, A. C., Aller, M. F., et al. 2021, *MNRAS*, **501**, 5997
- Türler, M., Courvoisier, T. J. L., & Paltani, S. 2000, *A&A*, **361**, 850
- Urry, C. M., Maraschi, L., Edelson, R., et al. 1993, *ApJ*, **411**, 614
- Urry, C. M., & Padovani, P. 1995, *PASP*, **107**, 803
- Weaver, Z. R., Jorstad, S. G., Marscher, A. P., et al. 2022, *ApJS*, **260**, 12
- Xie, G. Z., Liang, E. W., Zhou, S. B., et al. 2002, *MNRAS*, **334**, 459
- Xie, G. Z., Liu, H. T., Cha, G. W., et al. 2005, *AJ*, **130**, 2506
- Xie, G. Z., Yi, T. F., Li, H. Z., Zhou, S. B., & Chen, L. E. 2008, *AJ*, **135**, 2212
- Zechmeister, M., & Kürster, M. 2009, *A&A*, **496**, 577
- Zhang, B. K., Zhao, X. Y., Zhang, L., & Dai, B. Z. 2017, *ApJS*, **231**, 14